nature COMMUNICATIONS

ARTICLE

Received 28 Aug 2014 | Accepted 14 Jan 2015 | Published 17 Mar 2015

DOI: 10.1038/ncomms7292

OPEN

Oscillation of the velvet worm slime jet by passive hydrodynamic instability

Andrés Concha[1], Paula Mellado[1], Bernal Morera-Brenes[2], Cristiano Sampaio Costa[3], L. Mahadevan[4,5] & Julián Monge-Nájera[6]

The rapid squirt of a proteinaceous slime jet endows velvet worms (Onychophora) with a unique mechanism for defence from predators and for capturing prey by entangling them in a disordered web that immobilizes their target. However, to date, neither qualitative nor quantitative descriptions have been provided for this unique adaptation. Here we investigate the fast oscillatory motion of the oral papillae and the exiting liquid jet that oscillates with frequencies $f \sim 30$–60 Hz. Using anatomical images, high-speed videography, theoretical analysis and a physical simulacrum, we show that this fast oscillatory motion is the result of an elastohydrodynamic instability driven by the interplay between the elasticity of oral papillae and the fast unsteady flow during squirting. Our results demonstrate how passive strategies can be cleverly harnessed by organisms, while suggesting future oscillating microfluidic devices, as well as novel ways for micro and nanofibre production using bioinspired strategies.

---

[1] School of Engineering and Sciences, Adolfo Ibañez University, Diagonal las Torres 2640, Peñalolen, Santiago 7941169, Chile. [2] Laboratorio de Genética Evolutiva, Escuela de Ciencias Biológicas, Universidad Nacional de Costa Rica, 86-3000 Heredia, Costa Rica. [3] Department of Zoology, Institute of Bioscience, Universidade de Sao Paulo, Sao Paulo, Sao Paulo 11461, Brazil. [4] School of Engineering and Applied Sciences, Harvard University, Cambridge, Massachusetts 02138, USA. [5] Department of Physics, Harvard University, Cambridge, Massachusetts 02138, USA. [6] Tropical Biology, Universidad de Costa Rica, 2060 San José, Costa Rica. Correspondence and requests for materials should be addressed to A.C. (email: andres.concha@uai.cl) or to J.M.-N. (email: julian.monge@ucr.ac.cr).

Rapid motions in nature are seen in a variety of situations associated with escape and predation. Extreme examples include the chameleon tongue that uses an unusual muscle-spring configuration to capture prey[1], and the venus flytrap that stores elastic energy and uses an instability for the rapid closure of its leaf[2]. The velvet worm is an unusual example of how an organism projects itself by squirting a jet of slime in an oscillatory fashion, not only for capturing prey[3], but also for defence[4–8]. Animals use squirting mechanisms for elimination of waste products (for example, urination in vertebrates); reproduction (gamete expulsion); communication (for example, pheromone excretion in mammals); locomotion (for example, squids); defence (for example, horned lizards); and hunting (for example, archer fish)[9–13]. These jets are normally directed in a straight line. We are aware of only three exceptions: velvet worms (Phylum Onychophora), spitting spiders (*Scytodes* spp.) and spitting cobras (*Naja* spp.). Spitting spiders oscillate their fangs[14], and spitting cobras actively oscillate their heads[15]. Despite having been a subject of study for over a century, the mechanism underlying the rapid oscillatory squirting of slime by the velvet worm remains a mystery[4,16,17]. Indeed, Darwin even hypothesized the creation of the disordered web as a potential origin for the evolution of spider webs[18].

In this article, we demonstrate that the fast oscillations of the jet slime and papillae in Onychophora are the result of a syringe-like system that, by means of a geometric amplifier, allows for fast squirt using slow muscular contraction. This fast flow activates an elastohydrodynamical instability that explains the fast papilla oscillations during defence and attack. We present a physical simulacrum that reproduces the instability in the same range of parameters of the natural system opening new venues for self-supported microfluidic devices and applications[19–22].

Results and Discussion

Worm attack kinematics. To capture the dynamics of the squirting process, we filmed several worm attacks (Supplementary Movies 1–3). In Fig. 1a–d, we show a series of snapshots of an attack recorded using high-speed imaging (480 frames per second a.k.a. f.p.s.), with the average duration of a squirt for all specimens being $\Delta t_{\mathrm{ave}} = 0.064 \pm 0.005$ s (Supplementary Table I; Supplementary Note 2). By tracking the motion of the tip of the jet shown in Fig. 1 and Supplementary Fig. 2, as a function of time, we found that the typical jet speed $V \sim 3$–$5\ \mathrm{m\,s^{-1}}$. Furthermore, we see that the squirt does not remain oriented but instead sprays an entire region as shown in Fig. 1e. These measurements raise the natural question of the spatio-temporal evolution of the liquid jet and its control by the worm.

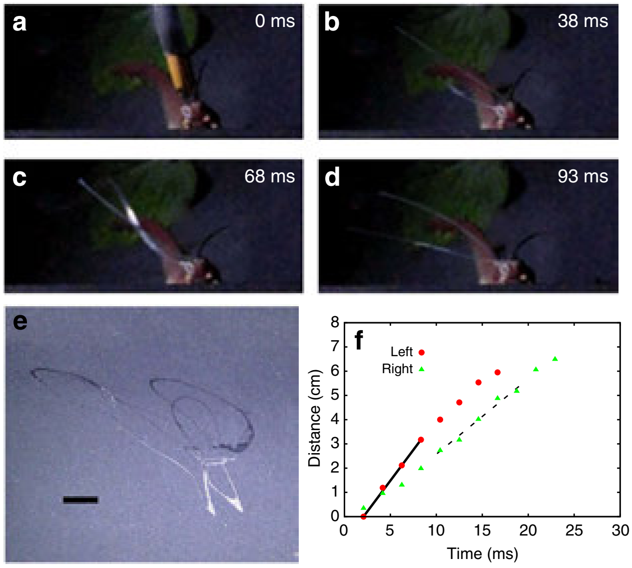

Figure 1 | Slime jet oscillations and jet speed during worm attack. Giant red velvet worm *Peripatus solorzanoi* used to record the squirting process. Full-body length is ∼17.5 cm. In **a**, a soft paintbrush used to activate its attack is shown, and it was digitally removed in the other snapshots for clarity. (**a**–**d**) Different stages of the attack recorded at 480 f.p.s. The active part of the attack is completed in $\Delta t_{\mathrm{squirt}} \sim 65$ ms. (**e**) Slime pattern generated on a wall of the foam tunnel used to keep worms at focal distance (scale bar, 1 cm). Three or more oscillations of the slime jet are the typical outcome. (**f**) Liquid jet tip position as a function of time for the squirt. For this data, we used two cameras: one at 30 f.p.s. and the other at 480 f.p.s. The two cameras configuration allowed us to compute the jet velocity. The solid line corresponds to a squirt speed of $V = 5.0\ \mathrm{m\,s^{-1}}$ and the dotted line to a squirt speed of $V = 3.2\ \mathrm{m\,s^{-1}}$. Solid red dots and green triangles correspond to left and right papilla, respectively.

Anatomy of the ejecting system. Actively controlled muscular action has long been invoked as the natural explanation for the spectacular way in which these worms quickly squirt slime and continues to be the favoured mechanism[16]. However, papillar oscillations are fast (Fig. 1; Supplementary Table 1 and Supplementary Note 2) in comparison with any other motion of the worm ($f_{\mathrm{papilla}}/f_{\mathrm{walking}} \sim 30$–$60$) and with known time scales (∼0.5 s) for the fastest muscles in the worm[23], suggesting a conceptual difficulty with this hypothesis. Therefore, we examined the anatomy of the whole-squirt system and surrounding tissues (Fig. 2; Supplementary Fig. 1). During squirting, the oral papilla extends from its folded shape to its full length (Fig. 2) of up to $L \sim 6$ mm (Supplementary Fig. 2). In Fig. 2a, we see a large reservoir region (re) where slime is stored and a narrow duct that ends at the oral papilla, a syringe-like geometry that facilitates the acceleration of the slime for the fast squirt. In Fig. 2a,b, we show that muscle fibres in the oral papilla are similar to those found in the legs, but fewer in number. Figure 2a,b and Supplementary Fig. 1 also show that muscular fibres found in papilla tissues are consistent with their directional function, with some being annular, typical of sphincter-like systems. The relaxed papilla has an accordion shape (Fig. 2c,d) that is unfolded just before the squirting process, and can thus be easily packed while also having an inhomogeneous bending rigidity, with soft spots that make papillae more pliable and susceptible to bending as slime is squirted.

Our anatomical findings are consistent with earlier evidence that slime papilla are modified limbs[24,25] with a nervous system similar to that in their legs[26]. Detailed descriptions of the Onychophora muscular system[23] show that the fastest muscles are located in the jaw with typical twitch time scales ∼0.5 s, which, while fast for this primitive worm, are nearly 25 times slower relative to the papillary oscillation time scale ∼20 ms. Given that the legs and the papillary muscles are even slower, consistent with the primitive nature of these worms[5,27,28], we are left with an obvious question—how are rapid changes in direction that occur over a time scale of a few milliseconds possible without the existence of any specialized rapid muscular actuation or neural control?

Physical mechanism. A way around this conundrum is to realize that a physical mechanism can drive the rapid and nearly chaotic oscillations of the papilla just as a garden hose pipe oscillates when water squirts out of it rapidly. Indeed, the inertial effects associated with the exiting fluid jet drive the elastic hose pipe to flutter, a subject that has been well studied experimentally and

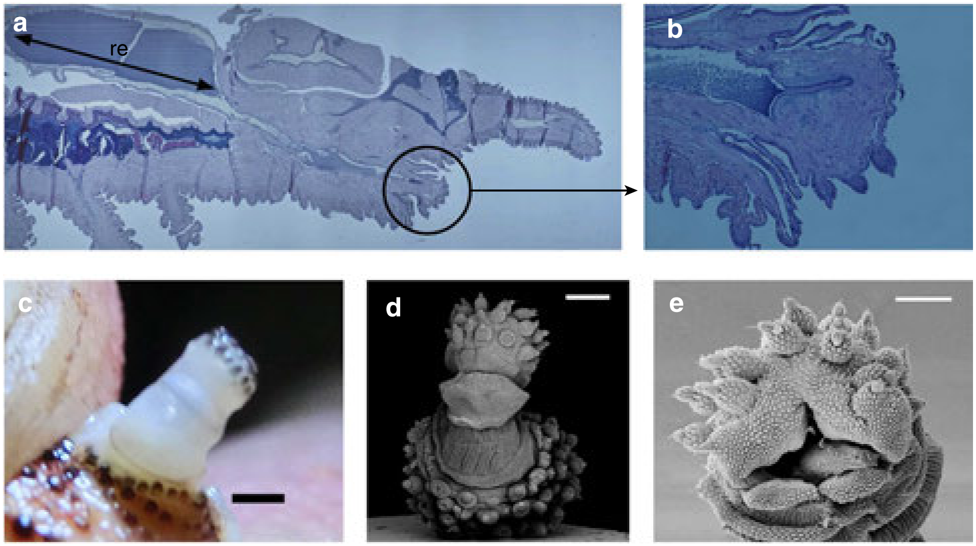

Figure 2 | Squirt system and papilla structure. (**a**) A haematoxylin and eosin-stained section of a *Peripatus solorzanoi*. The squirt system is composed of a large slime reservoir, re, whose length is depicted by a black arrow. The reservoir has a large diameter compared with the diameter of the duct that connects it with the oral papilla (black circle). (**b**) Longitudinal cut of an oral papilla of a *Peripatus solorzanoi*. Its wrinkled surface and sphincter-like tissues surrounding the inner duct are shown (scale 4 mm). The black substance inside the duct corresponds to remnants of the slime. (**c**) Structure of a fresh oral papilla (red *Peripatus solorzanoi*) when deployed. Its semi-transparent and wavy structure is apparent (scale bar, 1 mm). (**d**) Oral papilla accordion structure of a *Epiperipatus acacioi* (scale bar, 200 μm). In this case the hinged accordion structure is resolved by scanning electron microscopy (Leica Leo 440) taken at 15 kV after coating with gold (~ 20 nm) in a Denton Desk IV gold sputter model. This specimen was used to confirm that the accordion-like structure present in *Peripatus solorzanoi* is generic to Onychophora regardless of its size. (**e**) Opening of the oral papilla $D \sim 350\,\mu$m and $d \sim 200\,\mu$m (scale bar, 100 μm).

theoretically at the macroscale[29]. In the current microscopic setting, the interplay between fluid forces and the papilla elasticity produce the characteristic oscillatory waving motion used to capture prey, and obviate the need for any fast moving controlled muscles. However, this mechanism requires fluid inertia to play a critical destabilizing role, that is, the ratio of inertial to viscous forces characterized by the Reynolds number $\mathrm{Re} = VR/\nu > 1$ (where V is the characteristic fluid speed, ν the fluid kinematic viscosity and R the tube radius). In microfluidic geometries where typical sizes are small, unless the velocities are sufficiently large, inertial effects are unimportant.

Our microscopy studies (see Fig. 2a) show that the squirting system has a reservoir that contracts slowly driving the slime through a small duct that runs close to the centre of the oral papilla (Supplementary Figs 1 and 3). This geometric amplifier can lead to an increase in the speed during squirting. This is functionally similar to structures found in the chelicerae of spitting spiders[14], and suggests that this geometric amplifier mechanism could be relevant for a variety of other squirting organisms. Our observations are in contrast with previously reported studies[30] that have persisted into the modern literature[31], where no mention of the cross-section reduction has been made. Our micrographs show muscular structures (Fig. 2; Supplementary Fig. 1) around the slime reservoirs, which are functionally consistent with the contraction of this organ. These structures resemble the design of radial tires where a fibre network is used to reinforce the wall[32], consistent with detailed study of muscular fibres at reservoir level[33]. Measurements of the squirted volume (Supplementary Notes 1 and 3; Supplementary Fig. 4) and reservoir geometry show that the contraction ratio $\delta R_{\mathrm{re}}/R_{\mathrm{re}} < 0.03$ (with $R_{\mathrm{re}} \sim 2$ mm) changes in about 0.1 s, enough to produce speeds of $V \sim 5\,\mathrm{m\,s^{-1}}$, so that the Reynolds number $\mathrm{Re} \sim 2{,}700$ (Supplementary Note 6). Since we do not see perfect synchronization between liquid jets coming from different papilla (Fig. 1a–d; Supplementary Table I; Supplementary Movies 1 and 2), whole-body contraction as the main driving force in squirting[33] is unlikely.

This leads to the conclusion that the instability arises due to a competition between fluid inertia and elastic resistance. When a liquid moves steadily through a flexible pipe at small V, flow-induced damping prevents any oscillations from growing. For large enough V, centrifugal and Coriolis forces make the pipe unstable for fluid speeds $V > V_{\mathrm{c}}$. In the limit when the effects of gravity can be neglected (Supplementary Notes 5–7; Supplementary Fig. 8), a simple scaling argument allows us to estimate the frequency of oscillations f by balancing the stabilizing elastic bending resistance with the destabilizing inertial forces, that is,

$$EI/\lambda^4 \sim MVf/\lambda \sim MV^2/\lambda^2, \qquad (1)$$

where EI is the bending stiffness, $\lambda \sim 2L$ is the approximate oscillation wavelength for the cantilevered papilla and M is the mass density per unit length of the fluid in the pipe. This yields

$$f \sim \left(\frac{EI}{M}\right)^{1/2} \frac{1}{4L^2} \qquad (2)$$

Similarly, a typical speed scale can be estimated as $u_0 \sim f\lambda = (EI/M)^{1/2}(1/L)$. For the specimen shown in Supplementary Fig. 2, the oscillation frequency $f \sim 58$ Hz, papilla length $L = 6.0$ mm, papilla outer diameter $D = 1.0$ mm and papilla inner diameter $d = 0.5$ mm, from where $\beta \sim 0.25$. The measured frequency allows to estimate the effective Young's modulus of the papilla to be $E \sim 20$ kPa consistent with measurements using small magnets to pull the papilla that yields $E \sim 40$ kPa (Supplementary Table 2), and thence the typical speed $u_0 \sim 0.5\,\mathrm{m\,s^{-1}}$. The precise critical speed V_{c} depends on boundary conditions, which for the cantilever case gives $V_{\mathrm{c}} \sim 2\pi u_0 = 3\,\mathrm{m\,s^{-1}}$. At this critical speed, stability is lost via a Hopf type bifurcation[29] (see Supplementary Note 5, 6 for further information).

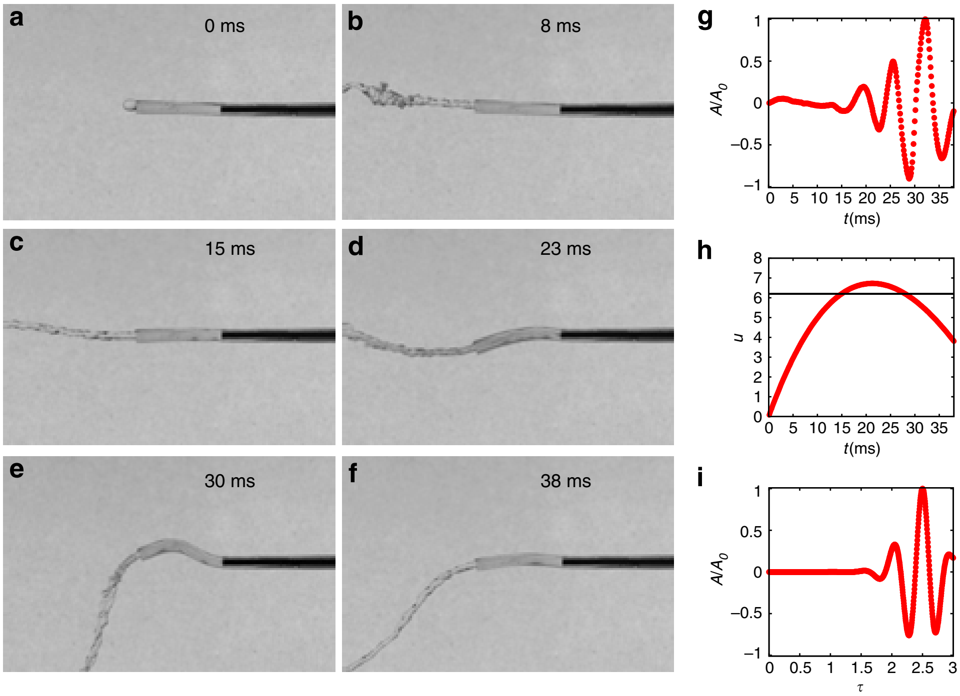

Figure 3 | Bioinspired physical simulacrum of the oral papilla. (**a**–**f**) A soft elastic cantilevered tube made out of polydimethylsiloxane (PDMS) becomes unstable as the fluid flowing through it increases its speed. Its height is $h = 1.42$ mm, width $w = 1.60$ mm, length $L = 9.5$ mm and hole diameter is 0.81 mm. The fluid used in this experiment was water. (**g**) The vertical motion of a point at the centre line of the hose close to the tip. As fluid speed is increased, oscillations develop and grow. The vertical axis is the dimensionless ratio between oscillation amplitude A and its maximum A_0. (**h**) During an emptying cycle, the fluid speed varies as a function of time, with the dimensionless speed $u \in [0.0, 6.9]$, with $u = V/u_0$. Horizontal black line depicts the theoretical threshold for instability in the case of steady flow. (**i**) Numerical simulations of the squirting dynamics associated with the dynamics of emptying shown in **h** using the governing equations. As in **g**, the vertical axis is the ratio between oscillation amplitude A and its maximum A_0. The horizontal axis is the dimensionless time $\tau = t/\tau_0$, where τ_0 is the bending time scale.

For unsteady flows, such as when the jet is being accelerated inside the flexible papilla, the fluid acceleration dv/dt can destabilize the system at even lower jet speeds (see Eqs. 3, 4 in Methods and Supplementary Fig. 8). Our measurements show that $V \sim 3.2$–$5.0\,\mathrm{m\,s^{-1}}$. Therefore, even without muscular action the papilla will become unstable due to a simple physical instability[29].

Synthetic simulacrum. To show that it is indeed possible to drive these oscillatory instabilities on small scales, we made a synthetic papilla out of a soft elastomer (see Methods) in the form of a flexible micropipe with a rectangular cross-section that defines an oscillation axis for its softest bending mode. Our pipe was moulded out of polydimethylsiloxane (PDMS) with a Young's modulus $E = 288$ kPa (Supplementary Figs 5–7; Supplementary Note 4), with thickness $h = 1.42$ mm, width $w = 1.60$ mm, inner diameter $d = 0.81$ mm and length $L = 9.5$ mm. Our model system is simpler than the natural one in at least two aspects: there is no roughness along the inner part of the duct or an external accordion-like geometry. Our experimental results (Fig. 3; Supplementary Fig. 5; Supplementary Note 5; Supplementary Movie 4) show that synthetic papilla becomes unstable and oscillates when the liquid reaches a speed of $V_c = 8.6\,\mathrm{m\,s^{-1}}$. This occurs in the same range of dimensionless parameters that for the natural organ in agreement with theoretical predictions [29], and shows that fast muscular action at the papillary level is unnecessary for oscillations. From measurements of external diameters (Fig. 2d), we found that $B = EI$ can locally change up to 1/10 of the stiffness corresponding to a uniform soft papilla of diameter D_0, showing that the accordion-like microstructure will lower V_c. Microtubes with accordion-like shapes made out of the same polymer were made varying the degree of external roughness. Our data shows that V_c lowers as we increase the amplitude of external roughness (Supplementary Note 6; Supplementary Fig. 9). The flow of liquids in pipes with inner roughness has been extensively studied[34,35]. The effect of inner pipe imperfections is to decrease the effective cross-section of the tube, as well as to anticipate the transition to turbulence[35]. All these effects together lower V_c, being the most important for the fluid regime described, the accordion-like modulations of the tube. Naturally, this experiment also suggests a prototype of a fluid driven micromechanical actuator[36–38].

Our observations, minimal theory and physical mimic show how velvet worms can spray a web rapidly to entangle their prey without resorting to a complex neuromuscular control strategy. Instead, they can simply harness the instability associated with rapid flow through a long soft nozzle that causes it and the exiting jet to oscillate. As this jet solidifies rapidly, it entraps the object dynamically. While there is a superficial similarity to spider webs, we see that here dynamics is of essence. Our findings and synthetic model might also pave the way to self-supported flexible microfluidic devices that can take advantage of similar instabilities to produce a variety of products such as microdrops[22,39–41], and non-woven fibre structures[19].

Methods

Sample collection. Specimens of *Peripatus solorzanoi* ($n = 3$) were collected in Guayacan, Siquirres, Costa Rica (10°3′21.38″ N, 83°32′44.04″ W, 500 m.a.s.l.). The specimen of *Epiperipatus acacioi* ($n = 1$) was collected in Minas Gerais, Brazil (20°22′44″ S, 43°32′55″ W, 1220 m.a.s.l.). The worms were housed in thermoplastic polystyrene (PS) terraria (370 × 240 × 280 mm) with a window covered with a metallic net as air vent. The temperature varied between 18 and 23 °C. The terraria received artificial illumination with standard daylight fluorescent lamps and had a 3–4-cm layer of leaf litter extracted from the original habitat of the specimens. This litter contained small invertebrates that are the natural food of the worms. The humidity in terraria was kept close to saturation all the time.

Optical microscopy. Tissues were fixed in 10% neutral-buffered formalin, processed with paraffin wax, sectioned at 6 µm and stained with haematoxylin and eosin for histological examination[42,43]. We used optical microscopy (Olympus BX41, Olympus camera E330-ADU1.2x, software Olympus Studio 2) to obtain the geometrical parameters involved in the reservoir and papilla duct, and to analyse the tissue structure at papilla and reservoir level.

Electron microscopy. Tissue samples kept in 70% alcohol were collected for scanning electron microscopy (SEM). Selected samples were re-hydrated and cleaned with a 3% solution of sodium hypochlorite (NaClO) and distilled water. They were dehydrated with an increasing alcoholic series: 30, 50, 70, 80, 90 and 100%, respectively. Later they were critical point dried in a Baltec CPD 030 and then coated with gold (~20 nm thick) in a Denton Desk IV gold sputter system. Specimens were imaged in a SEM (Leica, LEO 440). The morphological terminology for structures follows the one in ref. 44.

Image analysis. The measurement of squirting times (Supplementary Table 1) was performed using high-speed imaging of *P. solorzanoi* during squirt. We elicited the attack from the specimen using a gentle paint brush on its back. We have used a Casio EX-ZR200 camera capable of capturing colour movies up to 1,000 f.p.s. For speed measurement (Fig. 1f and Supplementary Fig. 2) we have used two cameras; one at 30 f.p.s. (lateral view) and a second high-speed camera (Casio EX-ZR200) at 480 f.p.s. The first camera allowed us to measure the distance between the worm and the high-speed camera, and with this data and the pixel location from the high-sped camera we computed the Euclidean distance between the papilla and the jet tip. The time evolution of the slime jet tip is shown in Supplementary Videos 1 and 2. To measure oscillations in the synthetic system, we have used a Phantom Miro 310 high-speed camera. We used up to 8,000 f.p.s., as in this case we are free to use high-intensity illumination to capture detailed information about the oscillation amplitude and frequency (Fig. 3 and Supplementary Fig. 8).

Micropipe fabrication and characterization. The fabrication of soft microtubes has been accomplished by standard fabrication techniques supplemented with some additional new techniques. The same method was used to fabricate rounded and rectangular cross-section channels. We began by fabricating a template of the channel of dimensions $w\sim 1$ mm (width), $h\sim 1$ mm (height) and $L\sim 30$ mm (length). This was done using a standard micro-mill ($\phi=1.0$ mm), on Plexiglas at extremely low feeding rates (5 mm per min) to avoid defects on the structure. A picture of the channels obtained is shown in Supplementary Fig. 5.

To make it easier to peel off the PDMS and the needle, we applied a soapy solution wash and let it dry; we repeated this procedure three times. The dried layer of soap[42] does not allow PDMS to stick either to the template or to the needle. We have been able to produce micropipes of inner diameters (d) from 800 µm down to 300 µm in a reproducible way. We obtained these microchannels by using commercial needles of different sizes, which we mounted on a scotch tape that is covering the end of the channels, Supplementary Fig. 5b. We punctured this film with the help of a microscope (for proper centring) and later we introduced the required size needle through that centring hole. When pulling the needle out of the PDMS channel, the thin soap layer worked as a lubricant allowing easy slip without damaging the inner tube surface, Supplementary Fig. 5. Later we cleaned the tube using isopropyl alcohol.

We mixed Sylgard 184 in a ratio 25:1 to get a soft polymer for the pipes. We hand mixed for 3 min and then used a centrifuge for mixing and bubble removal. We repeated the previous steps three times. Once completing this step, we carefully filled the templates using a syringe and then degassed the sample for 40–60 min. We checked for bubbles and possible leaking in the tape wall and then placed it in an oven at 70° C for 15 h. The PDMS removal was manually done. Some samples showed small lateral films attached to the main pipe. These leftovers when existent were removed by using a scalpel under the microscope. We double checked the integrity of the final micropipes after isopropyl alcohol and nitrogen cleaning by visual inspection under the microscope.

Model for fluid–papilla interactions. The motion of a pipe conveying fluid whose motions are restricted to be planar can be described by the following equation[29]:

$$\mathrm{EI}z^{(4)}+\left\{MV^2+\left[M\frac{\mathrm{d}V}{\mathrm{d}t}-(M+m)g\right](L-x)\right\}z^{(2)}$$
$$+2MV\frac{\partial^2 z}{\partial x\partial t}+(M+m)g\frac{\partial z}{\partial x}+v\frac{\partial z}{\partial t}+(M+m)\frac{\partial^2 z}{\partial t^2}=0 \qquad (3)$$

where $z(x,t)$ is the lateral motion of the beam centre line, M the fluid mass per unit length, EI the flexural rigidity, m is the tube mass per unit length, L is the tube length, V is the fluid speed, g acceleration of gravity and v is a phenomenological damping factor. We must emphasize that regardless of the cross-section shape the relevant quantity is the bending stiffness $B=\mathrm{EI}$.

The boundary conditions in this problem are $z(0,t)=0$, $z^{(1)}(0,t)=0$, $z^{(2)}(L,t)=0$ and $z^{(3)}(L,t)=0$. The relevant physical parameters needed to specify the parameter space for this problem can be found in equation (3) in a dimensionless form. This is easily achieved by using the dimensionless time and coordinates $\eta=\mathrm{z}/L$, $\chi=x/L$, $u=V/u_0$ and $\tau=t/\tau_0$. Where τ_0 is the bending time scale, and u_0 is a characteristic speed. The dimensionless equation reads:

$$\frac{\partial\eta^4}{\partial\chi^4}+\left\{u^2+\left(\beta^{1/2}\dot{u}(\tau)-\gamma\right)(1-\chi)\right\}\frac{\partial\eta^2}{\partial\chi^2}$$
$$+2\beta^{1/2}u(\tau)\frac{\partial^2\eta}{\partial\tau\partial\chi}+\gamma\frac{\partial\eta}{\partial\chi}+\sigma\frac{\partial\eta}{\partial\tau}+\frac{\partial^2\eta}{\partial\tau^2}=0 \qquad (4)$$

Numerical simulation. We have solved equation (4) using different numerical approaches. We did compare different methods as the coefficients of the PDE are not constant and may abruptly change as a function of time. The results we show were obtained using the Garlekin method. We use as basis the set of functions provided by the problem:

$$\mathscr{L}\psi=0 \qquad (5)$$

with the boundary conditions (BC) $\psi(0)=0$, $\psi'(0)=0$, $\psi^{(2)}(1)=0$ and $\psi^{(3)}(1)=0$. Where:

$$\mathscr{L}=\frac{\partial^4}{\partial\chi^4}+\frac{\partial^2}{\partial\tau^2} \qquad (6)$$

This problem endows us with a good expansion basis that fulfils the BC. After using the anzats,

$$\eta_{\mathrm{nmax}}(\chi,\tau)=\sum_{j=1}^{\mathrm{nmax}}\psi_j(\chi)q_j(\tau) \qquad (7)$$

and using the inner product properties of $\{\psi_j(\chi)\}_{j=1}^{\mathrm{nmax}}$ over the domain [0,1], we reduced equation (4) into a linear system using the first *nmax* basis functions. We emphasize that equation (4) captures well the onset of the instability. However, the oscillation amplitude does not saturate without including nonlinear terms in curvature[29]. To keep the model simple, we augmented equation (4) by a confining term $\alpha\eta^2$, and included the experimentally found damping σ (Supplementary Fig. 6).

References

1. Müller, U. & Kranenbarg, S. Power at the tip of the tongue. *Science* **304,** 217–219 (2004).
2. Forterre, Y., Skotheim, J., Dumais, J. & Mahadevan, L. How the venus flytrap snaps. *Nature* **433,** 421–425 (2005).
3. Read, V. & Hughes, R. Feeding behaviour and prey choice in macroperipatus torquatus (onychophora). *Proc. R. Soc. Lond. B* **230,** 483–506 (1987).
4. Belt, T. *The Naturalist in Nicaragua: a Narrative of a Residence at the Gold Mines of Chontales; Journeys in the Savannahs and Forests; with Observations on Animals and Plants in Reference to the Theory of Evolution of Living Forms* Vol. 561 (ICON Group International, 1888).
5. Bouvier, E. *Monographie Des Onychophores* Vol. I (Masson et Cie., 1905).
6. Claude-Joseph Observations Sur un peripate du chili. *Ann. Sci. Nat. Zool. Biol. Anim.* **Ser 10,** 285–299 (1928).
7. Alexander, A. Notes on onychophoran behavior. *Ann. Natal Mus.* **14,** 35–43 (1957).
8. Alexander, A. Peripatus: fierce little giant. *Ann. Natal Mus.* **14,** 35–43 (1958).
9. Demont, M. E. & Gosline, J. M. Mechanics of jet propulsion in the hydromedusan jellyfish, polyorchis pexicillatus: III. A natural resonating bell; the presence and importance of a resonant phenomenon in the locomotor structure. *J. Exp. Biol.* **134,** 347–361 (1988).
10. Anderson, E. J. & Grosenbaugh, M. A. Jet flow in steadily swimming adult squid. *J. Exp. Biol.* **208,** 1125–1146 (2005).
11. Dabiri, J. O. & Gharib, M. The role of optimal vortex formation in biological fluid transport. *Proc. R. Soc. B* **272,** 1557–1560 (2005).
12. Sherbrooke, W. C., Middendorf, III G. A. & Guyer, C. Blood-squirting variability in horned lizards (phrynosoma). *Copeia* **2001,** 1114–1122 (2001).
13. Vailati, A., Zinnato, L. & Cerbino, R. How archer fish achieve a powerful impact: hydrodynamic instability of a pulsed jet in toxotes jaculatrix. *PLoS ONE* **7,** e47867 (2012).
14. Suter, R. B. & Stratton, G. E. Spitting performance parameters and their biomechanical implications in the spitting spider, scytodes thoracica. *J. Insect Sci.* **9,** 1–15 (2009).
15. Young, B., Boetig, M. & Westhoff, G. Functional bases of the spatial dispersal of venom during cobra spitting. *Physiol. Biochem. Zool.* **82,** 80 (2009).
16. Morera-Brenes, B. & Monge-Nájera, J. A new giant species of placented worm and the mechanism by which onychophorans weave their nets (onychophora: Peripatidae). *Rev. Biol. Trop.* **58,** 1127–1142 (2010).
17. Haritos, V. *et al.* Harnessing disorder: onychophorans use highly unstructured proteins, not silks, for prey capture. *Proc. R. Soc. B* **277,** 3255–3263 (2010).

18. Moseley, H. On the structure and development of peripatus capensis. *Philos. Trans. R. Soc. Lond.* **164,** 757–782 (1874).
19. Mellado, P. *et al.* A simple model for nanofiber formation by rotary jet-spinning. *Appl. Phys. Lett.* **99,** 203107–203107 (2011).
20. Kim, H.-Y., Lee, M., Park, K. J., Kim, S. & Mahadevan, L. Nanopottery: coiling of electrospun polymer nanofibers. *Nano Lett.* **10,** 2138–2140 (2010).
21. Kang, E. *et al.* Digitally tunable physicochemical coding of material composition and topography in continuous microfibres. *Nat. Mater.* **10,** 877–883 (2011).
22. Eggers, J. & Villermaux, E. Physics of liquid jets. *Rep. Prog. Phys.* **71,** 036601 (2008).
23. Hoyle, G. & Del Castillo, J. Neuromuscular transmission in peripatus. *J. Exp. Biol.* **83,** 13–29 (1979).
24. Budd, G. E. A palaeontological solution to the arthropod head problem. *Nature* **417,** 271–275 (2002).
25. Scholtz, G. & Edgecombe, G. D. The evolution of arthropod heads: reconciling morphological, developmental and palaeontological evidence. *Dev. Genes Evol.* **216,** 395–415 (2006).
26. Mayer, G. & Whitington, P. M. Neural development in onychophora (velvet worms) suggests a step-wise evolution of segmentation in the nervous system of panarthropoda. *Dev. Biol.* **335,** 263–275 (2009).
27. Liu, J. *et al.* An armoured cambrian lobopodian from china with arthropod-like appendages. *Nature* **470,** 526–530 (2011).
28. Fortey, R. & Thomas, R. The case of the velvet worm. *Nature* **361,** 205–206 (1993).
29. Paidoussis, M. *Fluid-Structure Interactions: Slender Structures and Axial Flow* Vol. 1 (Academic press, 1998).
30. Manton, S. M. & Heatley, N. G. Studies on the onychophora. ii. the feeding, digestion, excretion, and food storage of peripatopsis with biochemical estimations and analyses. *Philos. Trans. R. Soc. Lond. B* **227,** 411–464 (1937).
31. Barnes, R. S. K., Calow, P. P., Olive, P., Golding, D. W. & Spicer, J. I. *The Invertebrates: a Synthesis* (Wiley-Blackwell, 2009).
32. Clark, S. K. *Mechanics of Pneumatic Tires* (US Department of Transportation, National Highway Traffic Safety Administration, 1981).
33. Baer, A. & Mayer, G. Comparative anatomy of slime glands in onychophora (velvet worms). *J. Morphol.* **273,** 1079–1088 (2012).
34. Nikuradse, J. *Laws of Flow in Rough Pipes* (National Advisory Committee for Aeronautics, Washington, 1950).
35. Kandlikar, S. G., Schmitt, D., Carrano, A. L. & Taylor, J. B. Characterization of surface roughness effects on pressure drop in single-phase flow in minichannels. *Phys. Fluids* **17,** 100606 (2005).
36. Whitesides, G. The origins and the future of microfluidics. *Nature* **442,** 368–373 (2006).
37. Leslie, D. C. *et al.* Frequency-specific flow control in microfluidic circuits with passive elastomeric features. *Nat. Phys.* **5,** 231–235 (2009).
38. Ho, C.-M. & Tai, Y.-C. Micro-electro-mechanical-systems (mems) and fluid flows. *Ann. Rev. Fluid Mech.* **30,** 579–612 (1998).
39. Kaufman, J. *et al.* Structured spheres generated by an in-fibre fluid instability. *Nature* **487,** 463–467 (2012).
40. Kong, T. *et al.* Droplet based microfluidic fabrication of designer microparticles for encapsulation applications. *Biomicrofluidics* **6,** 34104 (2012).
41. Yang, W., Duan, H., Li, C. & Deng, W. Crossover of varicose and whipping instabilities in electrified microjets. *Phys. Rev. Lett.* **112,** 054501 (2014).
42. Bonhomme, O., Liot, O., Biance, A.-L. & Bocquet, L. Soft nanofluidic transport in a soap film. *Phys. Rev. Lett.* **110,** 054502 (2013).
43. Santoro, M., Morales, J. A., Stacy, B. A. & Greiner, E. C. Rameshwarotrema uterocrescens trematode parasitism of the oesophageal glands in green sea turtles (chelonia mydas). *Veterinary Record.* **160,** 59–60 (2007).
44. de Sena Oliveira, I. *et al.* Unexplored character diversity in onychophora (velvet worms): a comparative study of three peripatid species. *PloS ONE* **7,** e51220 (2012).

Acknowledgements

A.C. and P.M. acknowledge partial support from Conicyt PAI 79112004. A.C. and P.M. were also partially supported by Fondecyt grants 11130075 and 11121397, respectively. B.M.-B. was partially supported by Universidad Nacional de Costa Rica, Project 0095-14. C.S.C. was partially supported by FAPESP 2011/20211-0 and 2012/02969-6. L.M. acknowledges the support of the MacArthur Foundation. A.C. thank Zhiyan Wei for sharing his insights about instabilities in flexible fibres and related phenomena. We also acknowledge S. Rica, J. Poupin, T. Ledger and B. Gonzalez for conversations and training, and K.Vega-Corrales for the help with operational duties in Costa Rica.

Author contributions

A.C. brought together the collaboration, designed and built experiments, performed imaging and numerical simulations. P.M. and A.C. performed the microfluidic experiments and carried out the fluid-dynamics analysis. L.M. proposed the link between the biological problem and the artificial one, suggested the physical mechanism. B.M.-B., J.M.-N. and C.S.C. provided the velvet worms, performed and interpreted microscopy, and carried out the biological research. All authors contributed in writing the paper.

Additional information

Supplementary Information accompanies this paper at http://www.nature.com/naturecommunications

Competing financial interests: The authors declare no competing financial interests.

Reprints and permission information is available online at http://npg.nature.com/reprintsandpermissions/

How to cite this article: Concha, A. *et al.* Oscillation of the velvet worm slime jet by passive hydrodynamic instability. *Nat. Commun.* 6:6292 doi: 10.1038/ncomms7292 (2015).

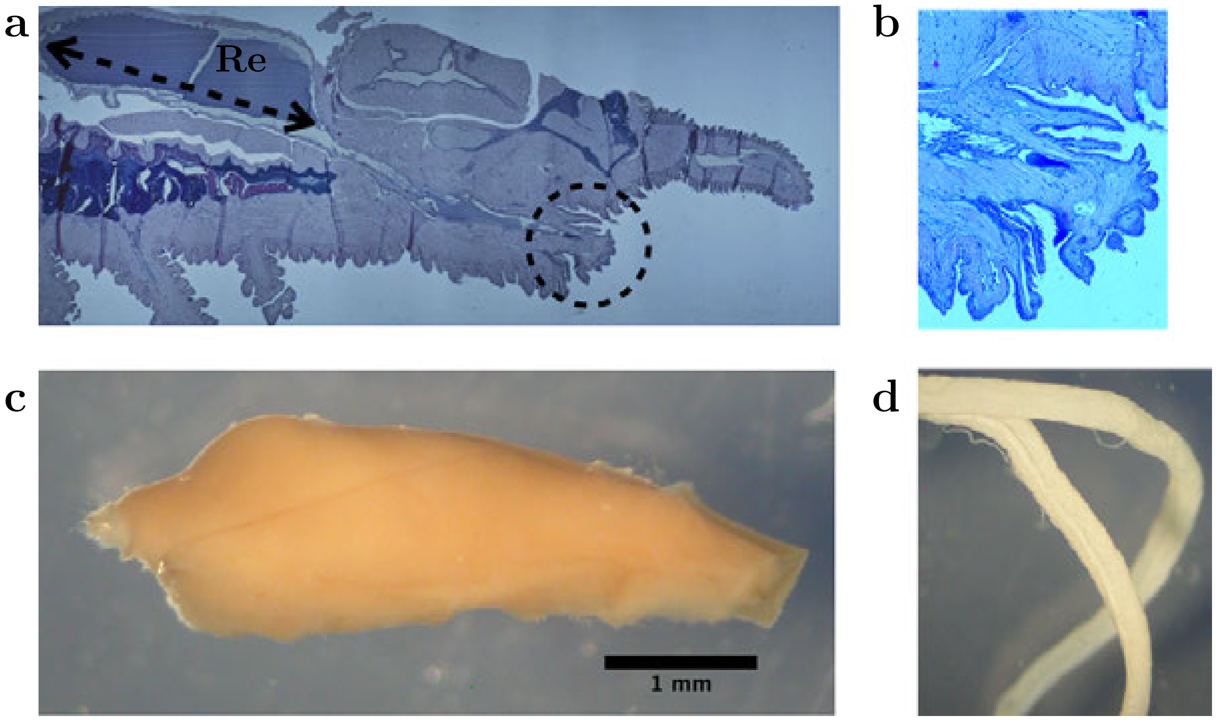

Supplementary Figure 1: **Optical Microscopy.** **a**, Longitudinal cut of a *Peripatus solorzanoi*. Dotted arrow mark the length $L = 13.0 \pm 0.2$ mm, of the widest part of an almost depleted reservoir, **Re**, (dark cylindrical area). Its diameter $D = 3.7 \pm 0.2$ mm. The reservoir becomes narrow and ends in the oral papilla (circled region). **b**, Zoom in of the oral papilla, circled region in Supplementary Fig.1**a**. We note that these dimensions are smaller than in the alive specimen as specimens contract when stored in formalin. Indeed, just after dissection the reservoir length was $L = 30 \pm 1$ mm. **c**, Solidified slime obtained from a different specimen. In this case $D = 1.9$ mm in the wider part. This 3D template clearly shows the difference between the narrow canal (leftmost region) and the center of the reservoir. **d**, Long reservoir showing muscular structure similar to the one reported by Baer *et al.*[1].

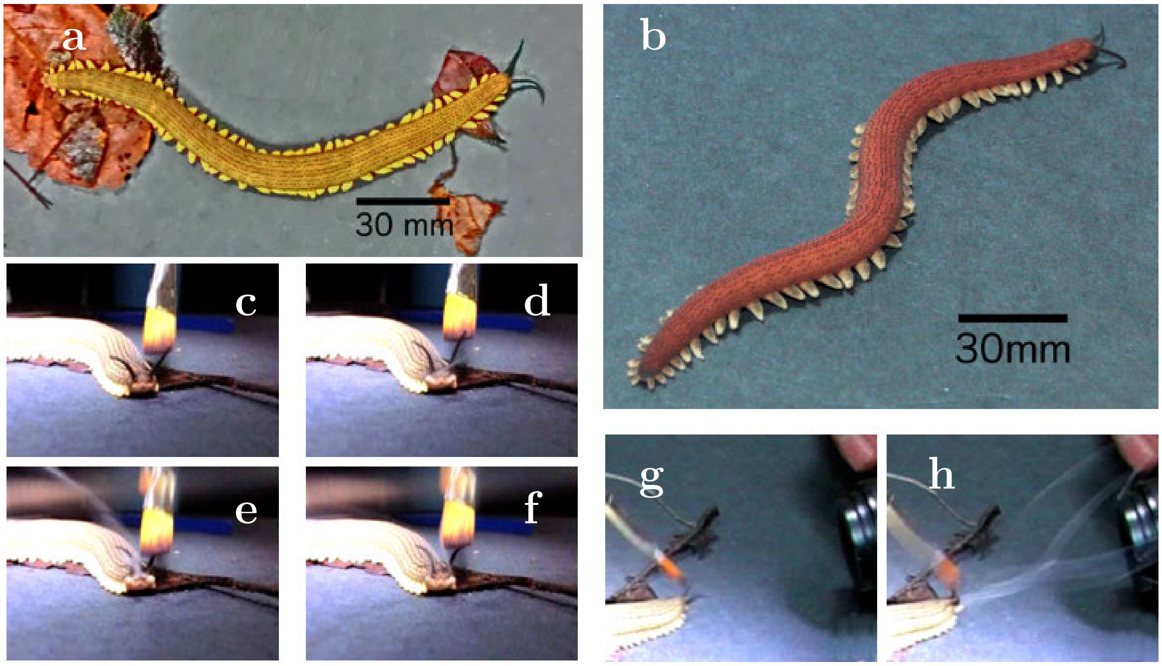

Supplementary Figure 2: **Worm attack and sizes.** **a**, *Peripatus solorzanoi* of sizes $\sim$ 18 cm, and **b** of size $\sim$ 17 cm are shown. **c**-**f**, Snapshots of a 480 fps (frames per second) video are shown (The attack was complete in $t_{squirt} \sim 60$ ms). To stimulate the attack we used a soft paintbrush, and light. **g**, **h**, side view of the attack taken with a 30 fps camera. Using information from both cameras we obtained data for Fig.1-f (Main text).

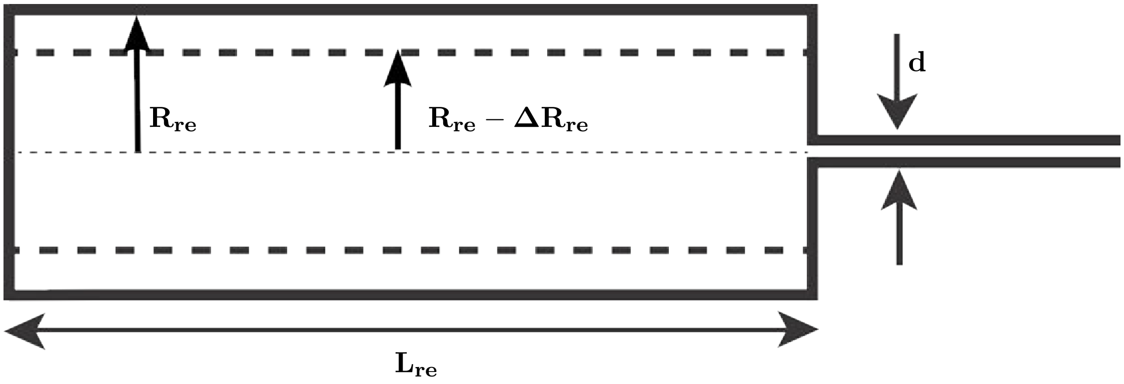

Supplementary Figure 3: **Syringe model diagram.** The big cylinder (solid line), of radius R_{re} represents the reservoir before contraction. After contraction the reservoir walls contract to a radius $R_{re} - \Delta R_{re}$. The small channel represents the canal through which the slime transits until reaching the oral papilla. The ability of the worm to squirt to very high speeds $V \sim 5$ m s^{-1} strongly depends on the ratio between reservoir and canal radius.

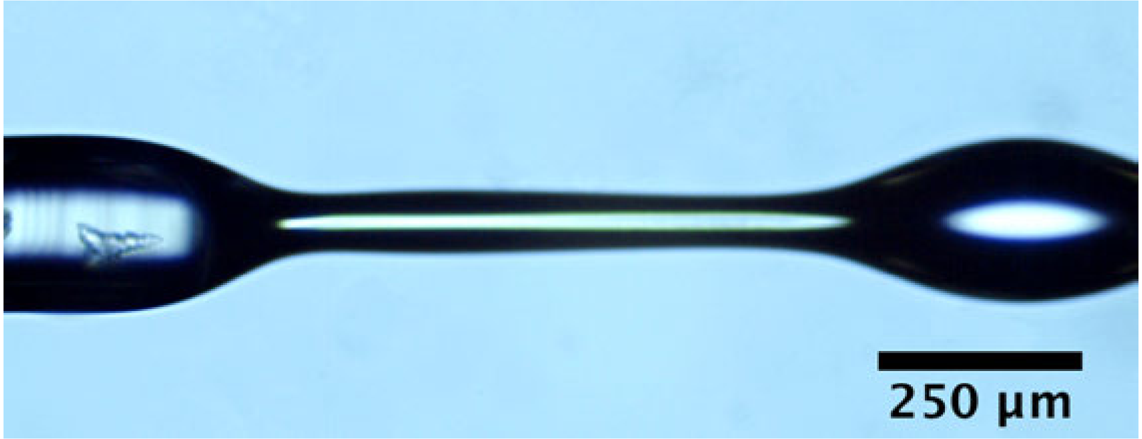

Supplementary Figure 4: **Fiber and beads.** Solidified jet (fiber) with typical structure shown across all specimens; a central fiber decorated by beads. These beads on a string effect is the consequence of the interplay between capillary, elastic, viscous, and inertial forces[2]. The beads on a string formation dynamics is cutoff by the drying process.

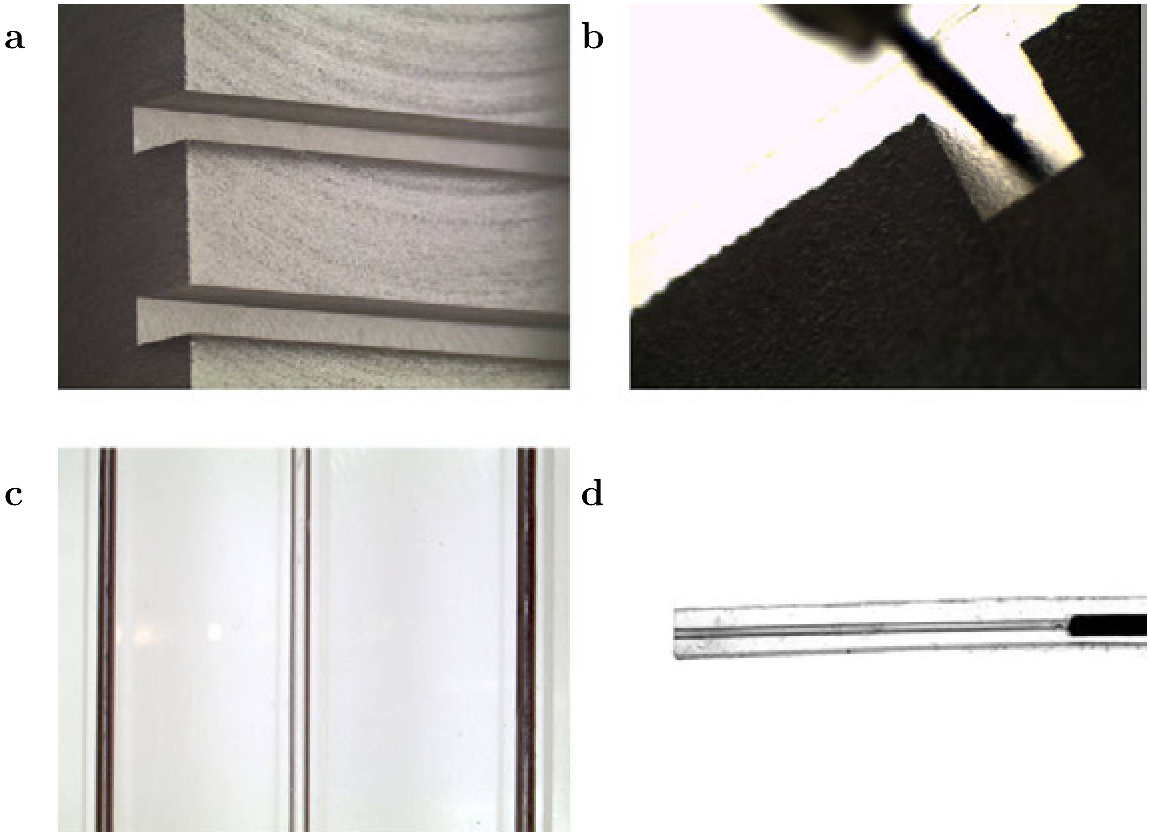

Supplementary Figure 5: **Template for micro-pipe production.** **a**, The acrylic template used to shape the micro-pipes. Channel width 1.6 mm, and depth 2 mm. **b**, Scotch tape centering technique used for holding the needles. Needle diameter 0.51 mm. **c**, Channels filled with PDMS and with and without needles. Needle diameter 0.81 mm. **d** After peeling off the channels and mounting the micro-pipe in a rigid rounded needle to form a cantilever. Needle diameter 0.51 mm, channel diameter 300 μm.

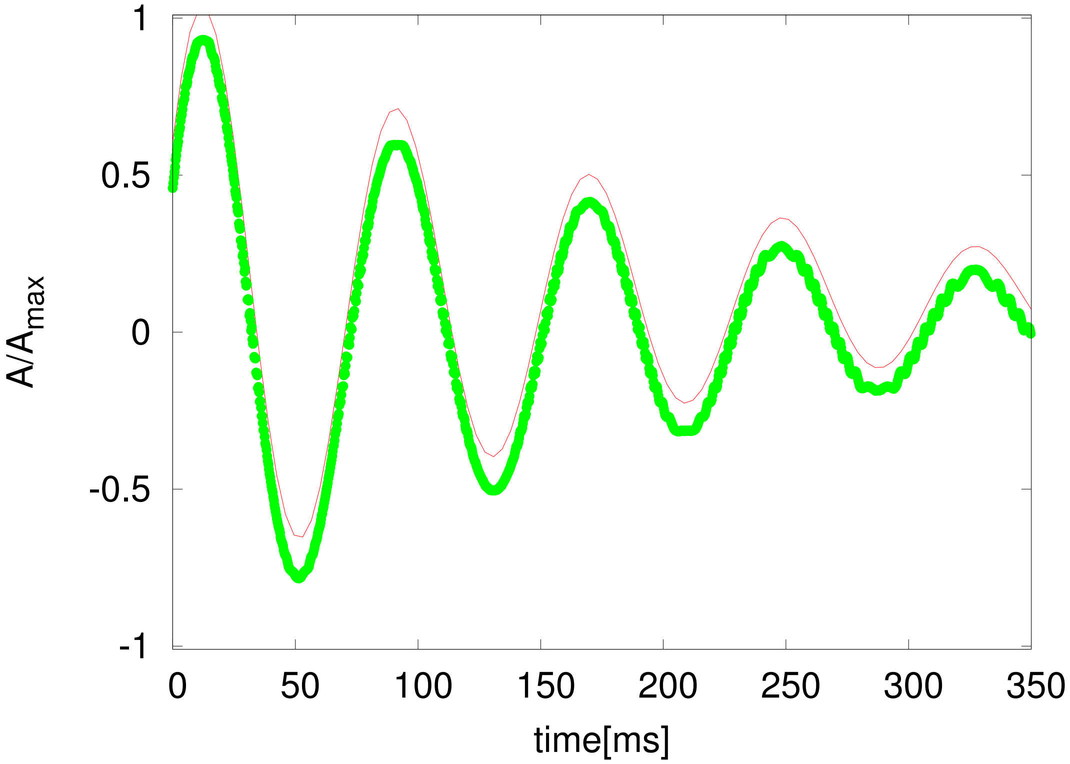

Supplementary Figure 6: **Free oscillations of the artificial papilla. a** After a slight perturbation, we recorded the damped oscillations of the cantilever. Imaging was done at 8000 fps. Experimental data (Green dots) were fitted to a damped dynamics $A = A_{max}e^{-\nu t}\cos(\Omega t + \delta)$ obtaining $\Omega = 79.78$ s^{-1}, $\delta = -1.04$, $\nu = 5.35$ s^{-1}. The red line is the best fit result were a small vertical offset was introduced for clarity.

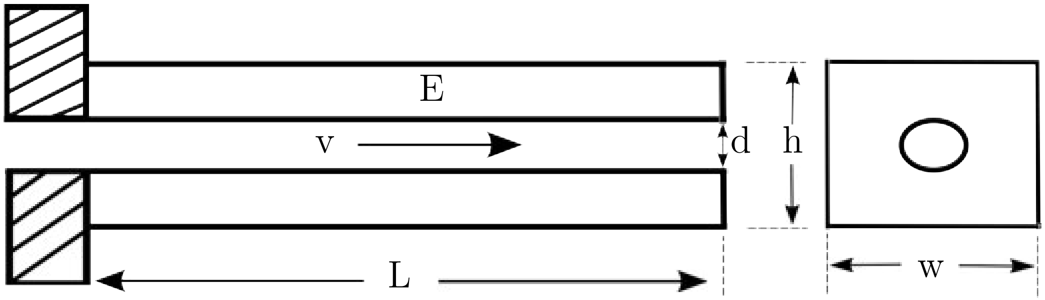

Supplementary Figure 7: **Synthetic papillae model.** A soft tube made out of Polydimethylsiloxane (PDMS) of Young's modulus, E. Its dimensions are d (inner diameter), h (tube height), w (tube width), L (papilla length), and V (liquid speed). In the experiment shown in Supplementary Movie 4, $L = 9.8$ mm, $w = 1.6$ mm, $h = 1.42$ mm, $u_0 = 1.4$ m s^{-1}, $\tau_0 = 0.014$ s.

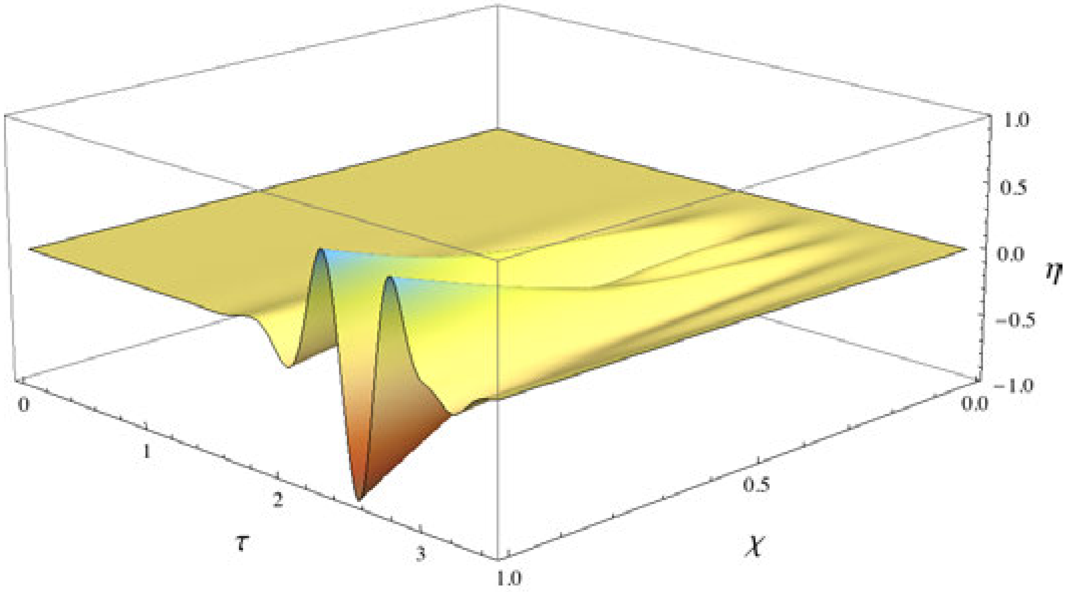

Supplementary Figure 8: **Spatio-temporal numerical evolution.** Numerical simulation result for artificial papilla motion. Results shown were obtained using Garlekin's method Eq. 3 (Main Text). Parameters used are $\beta = 0.24$, $u_{max} = 6.7$, $\tau_{max} = 3.0$. The χ-axis corresponds to the dimensionless coordinate along the papilla and the τ-axis corresponds to the dimensionless time of the system. The vertical axis corresponds to the dimensionless deformation amplitude η (See Methods).

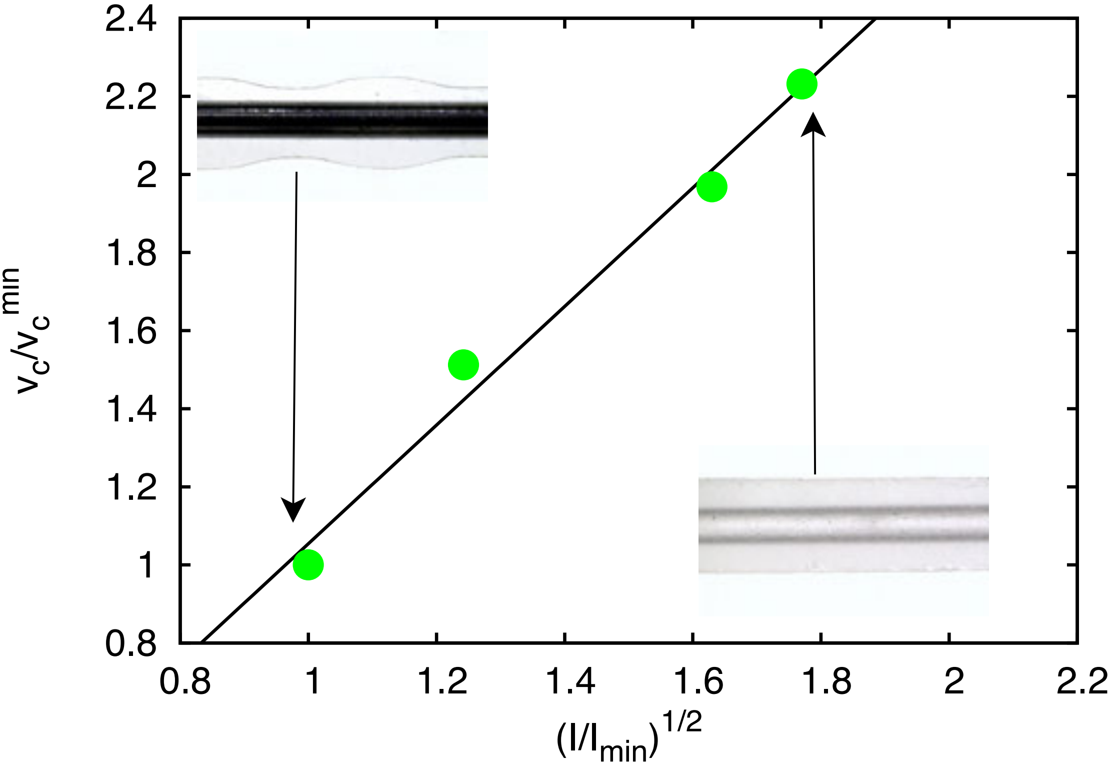

Supplementary Figure 9: **Critical velocity in accordion shaped micro tubes.** The critical velocity for pipe oscillations decreases when there are weak points. We show the rough micro tube before extracting the needle for clarity. The inner diameter is $d = 0.81$ mm. The horizontal axis corresponds to the square root of the ratio between the moment of inertia I, and the smallest local moment of the inertia for pipes used in this experiment I_{min}. The vertical axis is the ratio between the critical speed for a sample V_c, and the smallest critical speed V_c^{min} among all samples. The solid black line is the best linear fit consistent with our scaling arguments.

Specimen	fps	Active Phase	Δt [s]
Red 1	240	18	0.075
Red 1	240	13	0.054
Red2 (Left papilla)	480	30	0.063
Red2 (Right papilla)	480	37	0.077
White 1	480	25	0.052

Supplementary Table I: Squirt times obtained by using high speed video. Data from three giant specimens was obtained. Two red and one white. For specimen Red 2 we specify the papilla position as the liquid jet is not squirted at the same time in both papilla. The active phase column shows the number of fps where slime is actively being ejected from the papilla.

$\delta[10^{-4}\mathrm{m}]$	$F[10^{-5}\mathrm{N}]$	$E[\mathrm{kPa}]$
7.5	17	41.7
10	22	40.5

Supplementary Table II: Force-deflection data used to compute Young's modulus (Each measurement δ was repeated three times). One papilla was used from the red *Peripatus solorzanoi*. Papilla deflection δ was measured as function of the magnetic force F. This allowed us to find[3] the Young's modulus E.

Supplementary Note 1: Optical Microscopy.

We have used optical microscopy to obtain the geometry of the reservoir and papilla system, as well as to analyze the tissue structure at papilla and reservoir level.

In Supplementary Fig.1 **a** − **b**, a longitudinal cut at middle reservoir level clearly shows that the specimen anatomy has a large reservoir (**Re**) that ends in a narrow canal (black arrow). That narrow canal leads to the opening of the oral papilla (See Fig. 1 main text). This geometry is in contrast to previously reported anatomical studies[4] where no mention to the sudden cross section change has been reported. The inner dimensions and 3-D structure of the reservoirs were directly confirmed as a solidified template of it was found during dissection, Supplementary Fig.1 **c**. The Onychophora slime was found in a solid state confirming the dimensions obtained by microscopy. The ratio between D and d is ~ 20. This provides a simple, syringe-like mechanism that permits high squirting velocities at oral papilla level.

Supplementary Note 2: Average squirt times.

In Supplementary Fig.2 examples of Onychophora and the attack process are shown. Analyzing videos of the squirting process for several specimens we counted the number of frames (fps: frames per second) at which the liquid jet was being expelled from the oral papilla. Our results are summarized in Table I. From this data we get an average of $\Delta t_{ave} = 0.064 \pm 0.005$ s. As described in Table II, and consistent with field observations we have seen that right and left oral papillae may squirt at slightly different times, leaving the full body contraction hypothesis on weak grounds.

Supplementary Note 3: Slow muscular contraction for fast squirt.

As reported in Supplementary Note 1, the squirting mechanism is composed of a large reservoir that has strong muscle fibers in a configuration that makes the wall a contractile object[1]. This reservoir is connected to a narrow duct through which the slime is expelled. Based on this information the basic model of the squirting system is much alike a simple syringe (See Supplementary Fig.3). The slime is stored in a large cylinder (reservoir) of radius $\mathbf{R_{re}}$ and length $\mathbf{L_{re}}$ that radially contracts and pushes its content all the way through the narrow canal until it reaches the external opening located at the oral papilla (Supplementary Fig.1 **a-b** and Supplementary Fig. 3). As shown in Supplementary Fig. 3 (Geometry supported from our own observations and studied by Baer *et al.*) the whole mechanism is composed by the reservoir that contracts radially, and glands that produce the slime which transits to the reservoir. For the specimens used, the reservoir length $\mathbf{L_{re}} \sim 3 \cdot 10^{-2}$ m, and its radius has a typical value $\mathbf{R_{re}} \sim 2 \cdot 10^{-3}$ m. According to our measurements of the dry fiber and the organ opening (See Supplementary Figs. 1,4), the average fiber diameter is $d \sim 150$ μm. Using a high speed camera (240-480 fps) we have also measured the fiber propagation speed which is not constant but of order $V \sim 3 - 5$ m s^{-1}.

Using the above mentioned information we can ask how large the reservoir radial contraction should be in order to produce such a fast liquid squirting. This speed allows this slow moving worm to capture fast moving preys such as fireflies, and crickets between others. A cricket has a typical scape speed[5] of order 2 m s^{-1} .

We proceed to provide simple formulae that relate the vesicle geometry and jet dynamics considering an open geometry. The vesicle volume before and after contraction are $vol_i = \pi R_{re}^2 L_{re}$ and $vol_f = \pi \left(R_{re} - \Delta R_{re}\right)^2 L_{re}$, where ΔR_{re} is the change in the reservoir radius due to muscular contraction. Considering that $\Delta R_{re}/R_{re} \ll 1$ the volume of liquid expelled is $vol_i - vol_f \approx 2\pi R_{re} \Delta R_{re} L_{re}$ and that volume should be equal to the one of the squirted slime. In our experiments fiber length $\mathcal{C} \sim 60 \sim 10^{-2}$ m, and its mean radius $r \sim 75 \mu$m. (Supplementary Fig. 4). Volume conservation forces that $2\pi R_{re} \Delta R_{re} L_{re} = \pi r^2 \mathcal{C} \sim 10 \mu L$

from where the radial contraction can be computed as

$$\Delta R_{re} = \frac{r^2 \mathcal{C}}{2 R_{re} L_{re}} \tag{S1}$$

$$\Delta R_{re} = \frac{\left(75 \cdot 10^{-6}\right)^2 60 \cdot 10^{-2}}{2 \cdot 2.0 \cdot 10^{-3} \cdot 3 \cdot 10^{-2}} \approx 30 \cdot 10^{-6} \mathrm{m} \tag{S2}$$

This is the radial contraction of the reservoir. This means that the circular muscles must contract $\frac{\Delta R_{re}}{R_{re}} \sim 0.03$ in order to produce the needed change in volume. This contraction is well within biological capability[6–8].

The previous estimate is a consequence of overall volume conservation. However, the liquid slime is at a good approximation incompressible. Therefore, flow conservation holds. Balancing injected flow from the vesicle and squirting flow from the papilla we obtain:

$$V_{out} = \frac{2 R_{re} \Delta R_{re} L_{re}}{r^2 \tau} \tag{S3}$$

using Eq. S1 we find that an estimate for the squirting time is given by:

$$\tau = \frac{\mathcal{C}}{V_{out}} \tag{S4}$$

where τ is the typical time scale in which the liquid is actively expelled. Given that V_{out} has been measured from high speed movies (Supplementary Movies 1- 2) together with a standard videocamera for triangulation (Supplementary Movie 3), and ΔR_{re} was obtained from volume conservation (Eq. S1) we can extract the typical time scale for the vesicle contraction that allows the fast squirt .

$$\tau = \frac{60 \cdot 10^{-2}}{5} = 0.12 \ \mathrm{s} \tag{S5}$$

which is well within the reach of the muscles found in Onychophora, and consistent with experimental observations (Supplementary Movies 1 and 2). The radial contraction speed is quite slow $\Delta R_{re}/\tau \sim 3 \cdot 10^{-4}$ m s^{-1}.

Supplementary Note 4: Elastic properties measurements.

We determine the bending stiffness of the artificial papilla $B = EI$, and from that determine the Young's modulus, E, of the PDMS produced. We used a dynamical way to measure B. Free oscillation frequency, Ω, of a PDMS cantilever was measured recording at 8000 fps. Considering only the first eigenvalue λ_0 for the cantilever problem, we can find B using

$$\Omega = \left(\frac{\lambda_0}{L}\right)^2 \sqrt{\frac{B}{\mu}} \tag{S6}$$

where μ is the linear mass density, and L is the beam length. From the beam geometry we know that the moment of inertia is $I = wh^3/12$. We use this information and its relation with B to compute E of the PDMS sample. Experimental damped oscillations, and the best fit to $A(t) = A_{max}\cos(\Omega t + \delta)\exp(-\nu t)$ are shown in Supplementary Fig. 6 from where $E = 288$ kPa, and $\nu = 5.35$ s^{-1} is a damping factor.

In order to determine Papilla Young's Modulus (after dissection), we attached a small steel bearing ball (1mm in diameter) to the tip of an oral papilla, and used a magnet that was perpendicular to the sample to pull it. Thus, we deformed an oral papilla using magnetic forcing[3] in a free end cantilever configuration. In this case $F = 3\delta EIL^{-3}$, where F is the magnetic force, and $L = 3.0$ mm, the papilla length. We obtained $E \sim 40$ kPa (Supplementary Table II). This large value could be due to post-mortem rigidity combined with dry slime at the inner part of the tube.

Supplementary Note 5: Estimates of physical parameters.

The parameters that naturally emerge when obtaining the dimensionless Eq. 4 are: β, and γ corresponding to the ratio between the masses of liquid versus the total mass of the system, and the ratio between elastic forces and weight, respectively. Furthermore, typical speed u_0 and time τ_0 scales are needed to describe the dynamics of the system. We determine the values of these quantities to define the relevant parameter space in our experiments.

The mass parameter for a tube of circular cross section is:

$$\beta = \left(\frac{M}{m+M}\right) = \frac{1}{1+\left(\frac{D}{d}\right)^2} \tag{S7}$$

where $d \in \{0.15, 0.5\}$ mm, and $D \in \{0.3, 1.0\}$ mm giving $\beta \sim 0.25$ for the Onychophora specimens used in our experiments.

The characteristic velocity parameter is defined by:

$$u_0 = \left(\frac{EI}{M}\right)^{1/2} \frac{1}{L} \tag{S8}$$

for $d = 0.5$ mm, $D = 1.0$ mm, and $E = 40$ kPa resulting into $u_0 \approx 0.51$ m s^{-1}. We have measured jet speeds $V \in [3.2, 5.0]$ m s^{-1}. Therefore, the dimensionless parameter $u \in [6.3, 9.8]$.

$$\tau_0 = \left(\frac{m+M}{EI}\right)^{1/2} L^2 \tag{S9}$$

for $d = 0.5$ mm, $L = 6.0$ mm, and $m + M = (\rho D^2/4)$ Kg m^{-1}. Thus, the elastic time scale is $\tau_0 \approx 0.023$ s. The typical squirt time is $\Delta t_{ave} = 0.064$ s, from where the dimensionless squirt time is $\tau_{max} = \Delta t_{ave}/\tau_0 \sim 3.0$.

The parameter characterizing the influence of gravity in this system is

$$\gamma = \frac{(M+m)g}{EI} L^3 \tag{S10}$$

In our experiments, $\gamma \in [0.2, 0.8]$, showing that the role of gravity is negligible compared with the centrifugal term $\sim u^2$.

For the case of synthetic papilla we have chosen a rectangular cross section in order make visualization easier. In this case

$$\beta = \left(\frac{M}{m+M}\right) = \frac{\pi D^2}{4wh} \tag{S11}$$

in the experiment shown in Fig.3 (main text), $V_{max} = 9.4$ m s^{-1}, $h = 1.4$ mm, $w = 1.6$ mm, and $E = 288$ kPa. Resulting in physical parameters $\beta = 0.24$, $u_0 = 1.40$ m s^{-1}, $\tau_0 = 0.014$ s, and $\gamma = 0.21$. Dimensionless squirt time is $\tau_{max} = t_{max}/\tau_0 \sim 3$, and $u_{max} = 9.4/1.40 = 6.7$ comparable to the one found for the real specimen.

Using these parameters obtained from our experimental data we obtained a spatio-temporal plot shown in Supplementary Fig.8.

To further characterize the natural and artificial systems we introduce an elasto-fluidic Reynolds number as:

$$Re^{EF} = \frac{\rho u_0 d}{\mu} \tag{S12}$$

where ρ, and μ are the liquid density and the dynamical viscosity respectively. The dynamical viscosity of the Onychophora slime is unknown up to date. However, it should not be far from the value for water as before to enter in contact with air it is composed of 90 percent of water, and the remnant 10 percent is made out of proteins, sugars, lipids and nonylphenol[9]. Thus, our estimates for the natural system is:

$$Re^{EF} = \frac{10^3\text{kg m}^{-3} \cdot 0.51\text{m s}^{-1} \cdot 0.5 \cdot 10^{-3}\text{m}}{8.9 \cdot 10^{-4}\text{Pa s}} \sim 290 \tag{S13}$$

and for the artificial one

$$Re^{EF} = \frac{10^3\text{kg m}^{-3} \cdot 1.40\text{m s}^{-1} \cdot 0.81 \cdot 10^{-3}\text{m}}{8.9 \cdot 10^{-4}\text{Pa s}} \sim 1250 \tag{S14}$$

Supplementary Note 6: The effect of an accordion like external structure.

In order to analyze the effect of local changes in the bending stiffness EI we built micro tubes with rectangular cross section, but with variable width, w (Supplementary Fig. 7). The thickness was constant $h = 2.2$ mm. The modulation was a sinusoidal pattern where the maximum always reached the same point. That is, the maximum width of all samples was constant ($w = 2.0$ mm), but the local width of the pipe wall varied as shown in Supplementary Fig. 9.

In order to find V_c for these samples we repeated the procedure shown and described in Fig. 3 (Main text). The only difference is that images were acquired at 3200 fps for better image resolution.

The control parameter in Supplementary Fig. 9 is the ratio $(I/I_{min})^{1/2}$, where I_{min} is the smallest local moment of the inertia for pipes used in this experiment (See top left image Supplementary Fig. 9). We used this dimensionless parameter as we know that the typical speed in this system is:

$$u_0 = \left(\frac{EI}{M}\right)^{1/2} \frac{1}{L} \tag{S15}$$

Therefore, when keeping M, E, and L constant, $V_c \sim I^{1/2}$. Therefore, $V_c/V_{min} \sim (I_c/I_{min})^{1/2}$. We have used as reference $V_{min} = 4.7$ m s^{-1} corresponding to the lowest critical speed measured in the micro pipe with the largest amplitude of the modulation (See leftmost inset Supplementary Fig. 9). Our data shows the onset of the instability occurs at lower fluid speeds when weak points are present in the micro pipes.

1. Baer, A. & Mayer, G. Comparative anatomy of slime glands in onychophora (velvet worms). *Journal of morphology* **273**, 1079–1088 (2012).
2. Bhat, P. P. *et al.* Formation of beads-on-a-string structures during break-up of viscoelastic filaments. *Nature Physics* **6**, 625–631 (2010).
3. Savin, T. *et al.* On the growth and form of the gut. *Nature* **476**, 57–62 (2011).
4. Manton, S. M. & Heatley, N. G. Studies on the onychophora. ii. the feeding, digestion, excretion, and food storage of peripatopsis with biochemical estimations and analyses. *Philosophical Transactions of the Royal Society of London. Series B, Biological Sciences* **227**, 411–464 (1937).
5. Read, V. & Hughes, R. Feeding behaviour and prey choice in macroperipatus torquatus (onychophora). *Proceedings of the Royal society of London. Series B. Biological sciences* **230**, 483–506 (1987).
6. Kaya, M. & Higuchi, H. Nonlinear elasticity and an 8-nm working stroke of single myosin molecules in myofilaments. *Science* **329**, 686–689 (2010).
7. Tashiro, N. Mechanical properties of the longitudinal and circular muscle in the earthworm. *Journal of Experimental Biology* **55**, 101–110 (1971).
8. Hoyle, G. & Del Castillo, J. Neuromuscular transmission in peripatus. *The Journal of Experimental Biology* **83**, 13–29 (1979).
9. Benkendorff, K., Beardmore, K., Gooley, A., Packer, N. & Tait, N. Characterisation of the slime gland secretion from the peripatus, *Euperipatoides kanangrensis* (onychophora: Peripatopsidae). *Comparative Biochemistry and Physiology Part B: Biochemistry and Molecular Biology* **124**, 457–465 (1999).